

✓
NDB
2N-02-TM
023763

Numerical Prediction of Vortical Flow over Slender Delta Wings

J. A. Ekaterinaris and L. B. Schiff

Reprinted from

Journal of Aircraft

Volume 30, Number 6, November-December 1993, Pages 935-942



A publication of the
American Institute of Aeronautics and Astronautics, Inc.
370 L'Enfant Promenade, SW
Washington, DC 20024-2518

Numerical Prediction of Vortical Flow over Slender Delta Wings

J. A. Ekaterinaris* and Lewis B. Schiff†
NASA Ames Research Center, Moffett Field, California 94035

Three-dimensional Navier-Stokes numerical simulations are necessary to correctly predict the complex leeward-side flow characteristics over delta wings, including leading-edge separation, secondary separation, and vortex breakdown. This article presents Navier-Stokes solutions of subsonic vortical flow over a 75-deg sweep delta wing with a sharp leading edge. The sensitivity of the solution to the numerical scheme is examined using both a partially upwind scheme and a central-differencing scheme. The effect of numerical grid density is also investigated. An embedded grid approach is implemented to enable higher resolution in selected isolated flow regions, such as the leeward-side surface flow region, and the leading-edge vortical flow region.

Introduction

THE main feature of the flow over delta wings at an angle of attack is the separated flow along the leading edges, which form free shear layers rolling up around cores to form leading-edge vortices. The leading-edge vortices induce additional nonlinear lift, usually called vortex-induced lift. Increase in the angle of attack strengthens the vortices until eventually a sudden change occurs in the nature of the cores. This sudden change is known as vortex breakdown. In this article vortical flowfields, with and without vortex breakdown, over highly-swept sharp-edged delta wings are investigated.

Due to its importance to aerodynamics, the vortex breakdown over delta wings was explored in early experimental studies.^{1,2} Vortex breakdown was studied in controlled experiments on axisymmetric cylindrical vortices generated in confined tubes.³⁻⁶ Three types of vortex breakdown were observed for a cylindrical vortex,³ namely bubble breakdown, spiral breakdown, and double helix breakdown. Changes in the pressure gradient were found to have significant effects, thus a pressure increase downstream drives the breakdown upstream.

For flows over delta wings, bubble and spiral breakdown are encountered, depending on the angle of incidence and the sweep angle. Experimental studies of flows over a unity aspect ratio delta wing⁷ show that as the angle of attack increases, bubble-type breakdown precedes spiral-type vortex breakdown. The large suction pressure of the leading-edge vortex is diminished when vortex breakdown occurs with a subsequent loss of lift and nose-up pitching moment. After vortex breakdown, the vortex core is not re-established and the downstream end of the bubble usually is followed by a turbulent wake.

Experimental studies^{8,9} for flows over delta wings included surface and flowfield velocity and pressure measurements.

Recently, computational investigations of flow about delta wings at high angles of attack have been carried out¹⁰⁻¹³ using Navier-Stokes numerical simulations. The agreement of these numerical solutions with experimental data is good, and both spiral- and bubble-type vortex breakdowns were predicted. Previous numerical work,^{10,11} and the results of the present investigation, show that high grid resolution is required to resolve the complex leeward-side flow structure. The grid must be clustered close to the body surface to resolve the surface viscous flow. At high angles of attack vortex burst is observed and the flow pattern in the breakdown region becomes more complex. Although vortex breakdown is not a viscous-dominated process, grid resolution is required in the breakdown region in order to capture small-scale details of the flow, which otherwise are dissipated in a coarse grid. An embedded grid approach was employed and a solution was obtained with local grid refinement in the leeward-side region.

The objectives of the present work were to validate the solution by comparison with experiments, to conduct grid refinement studies, and to investigate alternative ways of obtaining accurate solutions with smaller computational effort by means of local grid refinement. The effect of the grid density on the numerical solutions was assessed. In addition, two alternate finite difference schemes were utilized: 1) a partially upwind scheme, and 2) a central-difference scheme. Solutions were obtained with single-block and zonal grids.

Computational Method

The conservation law form of the thin-layer compressible Navier-Stokes equations were used to obtain the numerical solution. The governing equations for a curvilinear coordinate system (ξ, η, ζ), are

$$\partial_t \hat{Q} + \partial_\xi \hat{F} + \partial_\eta \hat{G} + \partial_\zeta \hat{H} = Re^{-1} \partial_\zeta \hat{S} \quad (1)$$

In Eq. (1) all geometrical dimensions are normalized with the wing root chord length. The density is normalized with the freestream density ρ_∞ , and the velocities with the freestream speed of sound α_∞ .

The numerical integration is performed using both a partially flux-split numerical scheme¹⁴ and a numerical scheme with central differencing in all three directions.¹⁰ The upwinding is performed in the main flow direction with flux vector splitting, while central differencing is used in the other two spatial directions. The resulting two-factored

Presented as Paper 90-0102 at the AIAA 28th Aerospace Sciences Meeting, Reno, NV, Jan. 8-11, 1990; received April 24, 1990; revision received Oct. 10, 1992; accepted for publication Oct. 10, 1992. Copyright © 1990 by the American Institute of Aeronautics and Astronautics, Inc. No copyright is asserted in the United States under Title 17, U.S. Code. The U.S. Government has a royalty-free license to exercise all rights under the copyright claimed herein for Governmental purposes. All other rights are reserved by the copyright owner.

*Adjunct Research Professor, Navy-NASA Joint Institute of Aeronautics. Member AIAA.

†Special Assistant for High Alpha Technology. Associate Fellow AIAA.

algorithm is

$$\begin{aligned}
 & [I + h\delta_\xi^b(A^+)^n + h\delta_\zeta C^n - hRe^{-1}\delta_\zeta J^{-1}M^nJ - D_{i|\xi}] \\
 & \times [I + h\delta_\xi^b(A^-)^n + h\delta_\eta B^n - D_{i|\eta}]\Delta q^n \\
 & = -\Delta t\{\delta_\xi^b[(F^+)^n - F_\infty^n] + \delta_\xi^b[(F^-)^n - F_\infty^n] \\
 & + \delta_\eta(G^n - G_\infty) + \delta_\zeta(H^n - H_\infty) \\
 & + Re^{-1}\delta_\zeta(S^n - S_\infty)\} - (D_{e|\eta} + D_{e|\zeta})
 \end{aligned} \quad (2)$$

The central-differencing scheme employs the diagonalized form of the Beam-Warming algorithm. The factorized form of this numerical scheme is

$$\begin{aligned}
 & (I + h\delta_\xi A^n - D_{i|\xi})(I + h\delta_\eta B^n - D_{i|\eta}) \\
 & \times (I + h\delta_\zeta C^n - D_{i|\zeta} - hRe^{-1}\delta_\zeta J^{-1}M^nJ)\Delta q^n \\
 & = -h(\delta_\xi E^n + \delta_\eta F^n + \delta_\zeta G^n - Re^{-1}\delta_\zeta S^n) \\
 & - [D_{e|\xi} + D_{e|\eta} + D_{e|\zeta}]
 \end{aligned} \quad (3)$$

In Eqs. (2) and (3), D_e are the explicit dissipation terms that are used along the directions where central differencing is employed, and D_i are the implicit dissipation terms that are added for numerical stability. Steady aerodynamic flows at moderate subsonic speed ($M = 0.3$), such as that of the present study, do not contain shock waves and can be predicted quite well by a central-difference scheme, augmented by dissipation terms. The dissipation terms used are a combination of second- and fourth-order terms. The implicit and explicit dissipation terms are computed as suggested in Ref. 15.

Grid Generation

A spherical-type grid (or C-O grid), and a cylindrical-type grid (or H-O grid) were used. Sample spherical and cylindrical grids are shown in Figs. 1 and 2, respectively. A three-dimensional hyperbolic grid generation technique¹⁶ was used for field grid generation. Both grid configurations provided grid clustering along the axial direction, at the apex region, in the trailing edge, and the near wake region (see Figs. 1 and 2). The grid points along the spanwise direction were concentrated on the leeward side, especially in the vicinity of the sharp leading edge. The grid was clustered normal to the body surface to resolve viscous layers. The first point above the body surface was located at a distance d , $d = 0.00002$ nondimensional unit lengths. The outer grid boundaries were located 2–2.5 root chord lengths away from the body surface. Only half-body solutions were obtained, with symmetry conditions imposed at the angle-of-attack plane. The highest grid

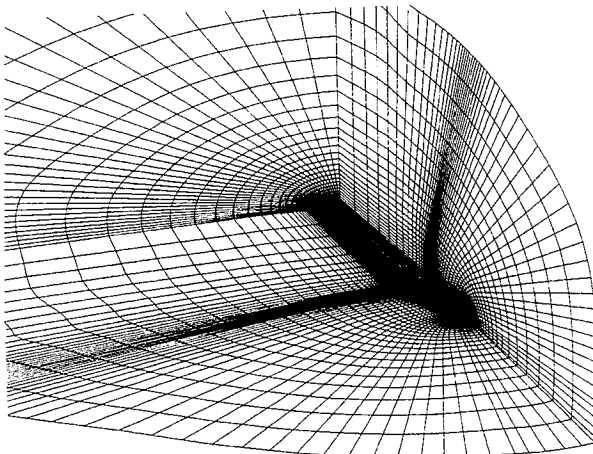


Fig. 1 Spherical grid over delta wing.

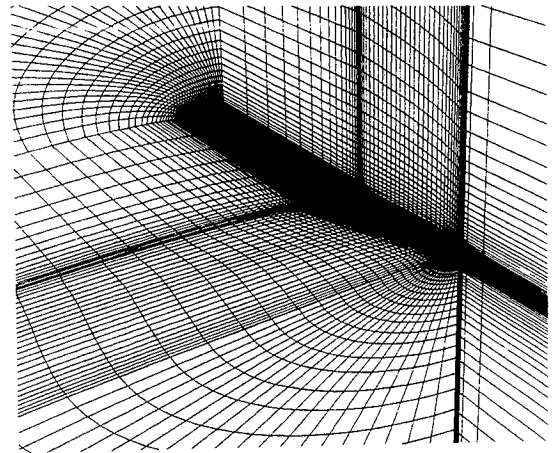


Fig. 2 Cylindrical grid over delta wing.

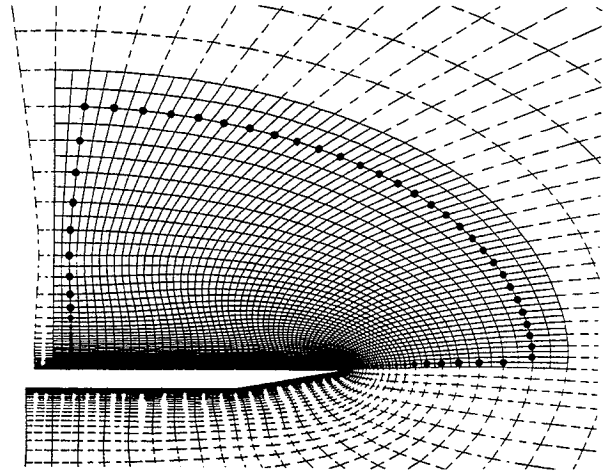


Fig. 3 Cross-sectional view of the computational mesh demonstrating the refined embedded grid and the interpolation points.

density used was $112 \times 105 \times 70$ points along the axial ξ , circumferential η , and normal ζ directions, respectively. The surface definition for the body used a bevel at the trailing edge that was different from the geometry of the experimental model.

Flows were computed with embedded grids using the chimera scheme^{17,18} which enables solutions with several overlapping grids. A selected flow region of the overall physical domain grid (global grid) in which higher resolution is required was identified and interpolated along one or all coordinate directions. The resulting grid is called an embedded grid. The cross-sectional view shown in Fig. 3 indicates the overlap region between the two grids and the points which were used to transmit information from one grid to the other. The chimera scheme was also applied for zonal grids.

With the chimera scheme the governing equations are advanced in time sequentially, first for the global grid and then for the embedded grid. The flow variables at the interface boundaries are obtained by simple interpolation of the global-grid solution. In those cases where some boundary of the refined grid coincides with a physical boundary, such as a solid wall, appropriate boundary conditions are applied. This procedure is repeated and the solution is advanced in time towards convergence to a steady state.

Results and Discussion

Computations were performed for flows over a 75-deg sweep ($AR = 1.07$) delta wing. Flow measurements for this wing geometry have been performed by Hummel⁸ and Kjølgaard and Sellers.⁹ In both reports detailed results are available at $\alpha = 20.5$ -deg angle of attack. Solutions were obtained at the

experimental flow conditions for $\alpha = 20.5$ deg and several higher angles of incidence in order to investigate the effect of the variation of the angle of attack on the flow structure.

Flow Without Vortex Breakdown

The solution for the flow at 20.5-deg angle of attack was chosen to examine the effects of grid density, grid topology, and the numerical scheme on the computed results. The zonal and embedded grid approach results were also compared with the single-block grid solutions. All computations for the 75-deg sweep delta wing were performed (except where noted) using the axially flux-split algorithm. The results were compared with the available measurements of Refs. 8 and 9. In Ref. 9, detailed off-surface laser Doppler velocimeter (LDV) measurements were made in the BART facility at NASA Langley on a 75-deg sweep model whose geometry matched that of the present computations. Flow conditions were $M_\infty = 0.3$ and Reynolds number (based on root chord) $Re_c = 1 \times 10^6$. Hummel⁸ obtained surface pressure measurements on a 76-deg sweep wing whose geometry was similar to the BART model, differing primarily on the windward side near the trailing edge. In Hummel's experiment the flow Reynolds number was $Re_c = 0.9 \times 10^6$ ($M_\infty \approx 0.05$). Since Reynolds number has only small effects for a sharp-edged wing, and compressibility effects are also small, Hummel's experimental results were compared to computations made at $M_\infty = 0.3$ and $Re_c = 1.0 \times 10^6$. The computed flow was assumed to be laminar. A sequence of comparisons of the computed solutions with the single-block, the zonal, and the embedded grid approach was conducted in order to show the validity of these approaches for vortical flows over delta wings. The experimental data and the computed solution with the finest grid density were used for subsequent comparisons. The fine single-block grid solution is validated first by comparison with experimental measurements.

Comparison with Experiment

The accuracy of the numerical method is evaluated by comparing the results obtained with the finest ($112 \times 105 \times 70$ point spherical topology) grid for the flow at an angle-of-attack $\alpha = 20.5$ deg with available experimental data. The computed surface pressure coefficients at different axial locations ($x/c = 0.3, 0.5, 0.7$, and 0.9) are compared with the results of measurements from Ref. 8 in Fig. 4. Good agreement was obtained for the windward-side flow except at the location $x/c = 0.9$ where the geometry used in the numerical simulation has a bevel at the trailing edge which does not match the geometry of the experimental model. The com-

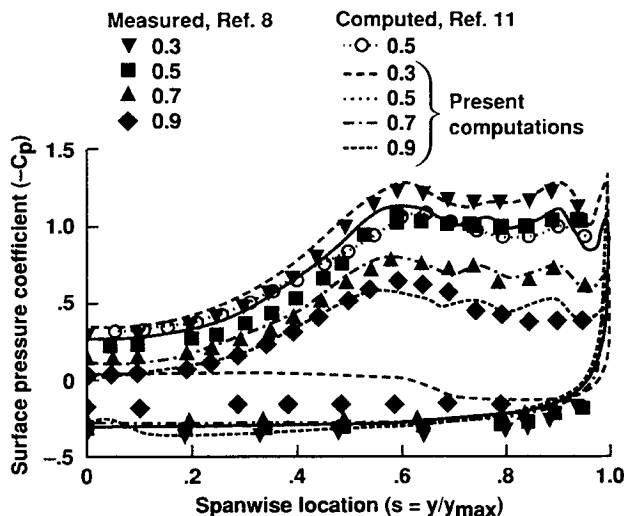


Fig. 4 Surface pressure coefficient: $M_\infty = 0.3$, $\alpha = 20.5$ deg, $Re_c = 1 \times 10^6$, with $112 \times 105 \times 70$ spherical grid.

puted surface pressure coefficients at the leeward side show an overall reasonable agreement with the results of measurements except for the last station $x/c = 0.9$. The suction peak caused by the primary vortex is closely predicted, while the suction peak caused by the secondary vortex is overpredicted. The discrepancy observed near the trailing edge ($x/c = 0.9$) may be due to the differences between the computational and experimental geometries, and the presence in the experiments of leeward-side flow transition. Also shown in Fig. 4 is the computed leeward-side pressure distribution of Ref. 11, at $x/c = 0.5$, obtained using a $65 \times 129 \times 65$ point grid. This solution shows the same trends as those of the present solution. Reasonably good agreement is found between the computed and experimental results for this case at all axial stations (with the exception of $x/c = 0.9$). Therefore, in examining

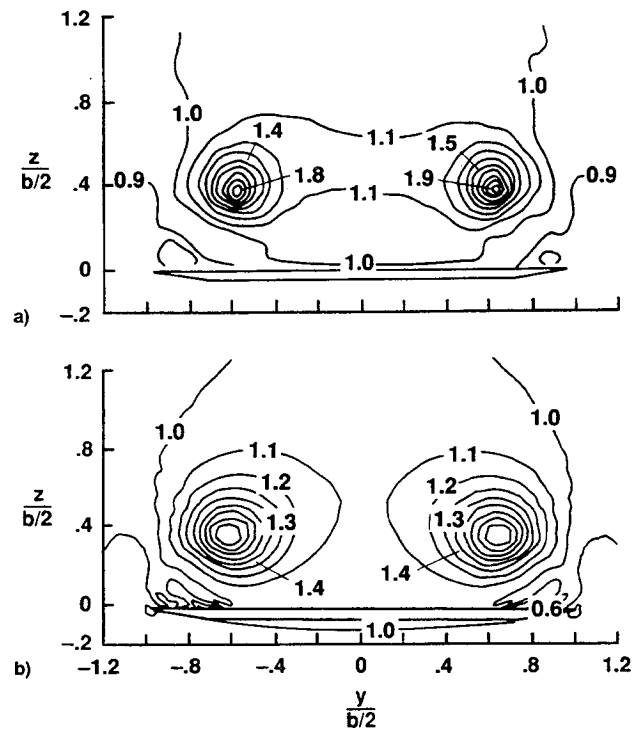


Fig. 5 Axial velocity contours in the $\xi = \text{const}$ crossflow surface at $x/c = 0.9$: $M_\infty = 0.3$, $\alpha = 20.5$ deg, $Re_c = 1 \times 10^6$, with $112 \times 105 \times 70$ spherical grid: a) measured, b) computed.

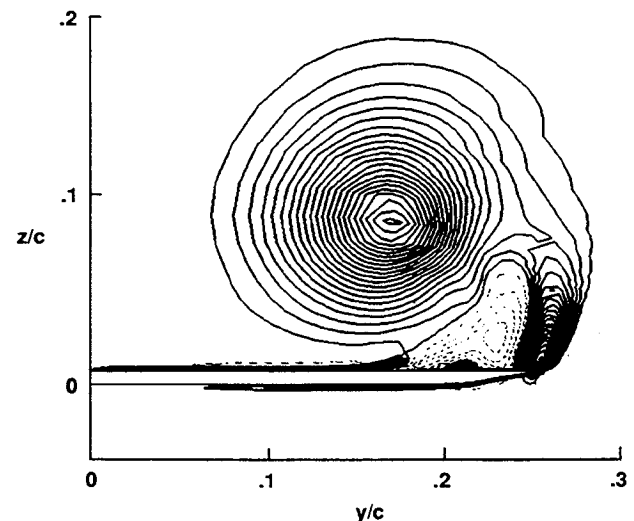


Fig. 6 Helicity contours in the $\xi = \text{const}$ crossflow plane at $x/c = 0.9$: $M_\infty = 0.3$, $\alpha = 20.5$ deg, $Re_c = 1 \times 10^6$, with $112 \times 105 \times 70$ spherical grid.

the effects of grid resolution, zonal grids, grid topology, and the numerical algorithm on the computational results, we focus on the behavior of the two solutions at $x/c = 0.5$.

The off-surface axial velocity distribution predicted from the $112 \times 105 \times 70$ spherical grid solution in a crossflow plane at $x/c = 0.9$ is compared with results of the measurements of Ref. 9 in Fig. 5. The location of the vortex core is predicted closely, and the computed axial velocity distribution closely matches the experimental results. The computed results are shown in a normal $\xi = \text{const}$ surface. The other two velocity components (not shown here) also agree with the experimental results. The overall view of the vortical flow over the leeward side at the same axial location $x/c = 0.9$ is shown in Fig. 6 using helicity contours. A good representation of the vortical flowfield can be obtained by use of the helicity density, as was discussed in Ref. 19. Helicity H is a scalar, the inner product of the velocity and vorticity vectors $H = \mathbf{V} \cdot \boldsymbol{\Omega}$. The helicity contour plot shows the extent of the vortical region and the vortex core as the location where the helicity attains a local maximum value. The helicity contour plot of Fig. 6 shows the extent of the vortical field and the primary, secondary, and tertiary vortex cores. In addition, the secondary and tertiary separation lines are indicated by sign reversal of the helicity at the body surface (here negative helicity values are shown with dashed lines).

Effect of Grid Resolution

The results obtained with the finest $112 \times 105 \times 70$ point spherical single-block grid adequately capture the important flow characteristics and agree with the experiments. It is important to have a grid fine enough to resolve the pertinent physics while keeping the total number of points to a minimum due to long execution time requirements. Comparisons of the solutions obtained on the largest $112 \times 105 \times 70$ point spherical topology grid and a grid having a reduced axial resolution of $56 \times 105 \times 70$ points do not indicate differences in the flowfield structure. The surface pressure coefficients of both solutions at $x/c = 0.5$ are shown in Fig. 7, and are in good agreement. Doubling the grid resolution in the axial direction from 56 to 112 is not expected to have a very significant effect on the accuracy of the solution, because at this moderate angle of attack the flow is approximately conical, and therefore, the axial gradients are small. The surface pressure coefficient at $x/c = 0.5$ predicted by the solutions with coarser spherical grids are compared in the same figure with the fine-grid results and the experiments. The solution obtained on a $56 \times 54 \times 70$ point grid shows some differences from the finer grid resolution results. The need for adequate grid resolution in the body normal direction is particularly critical. The deviation from the measured values is larger for grids having coarse normal resolution and the suction peak due to the secondary

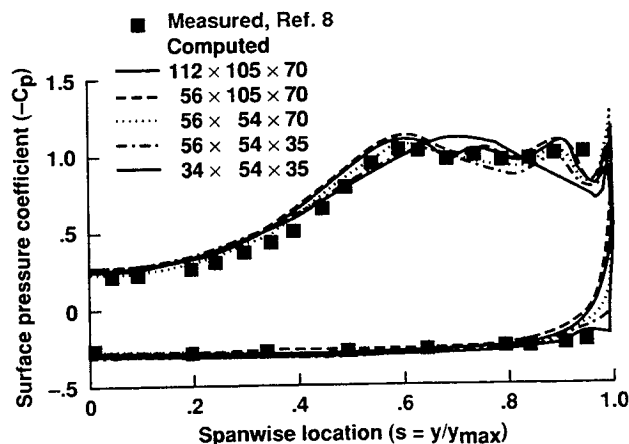


Fig. 7 Effect of the grid density on the prediction of surface pressure coefficient: $M_\infty = 0.3$, $\alpha = 20.5^\circ$, $Re_c = 1 \times 10^6$.

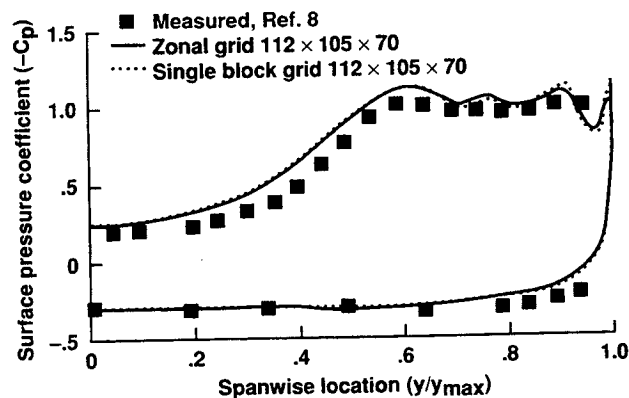


Fig. 8 Surface pressure coefficient: $M_\infty = 0.3$, $\alpha = 20.5^\circ$, $Re_c = 1 \times 10^6$, with $112 \times 105 \times 70$ spherical single-block and zonal grids.

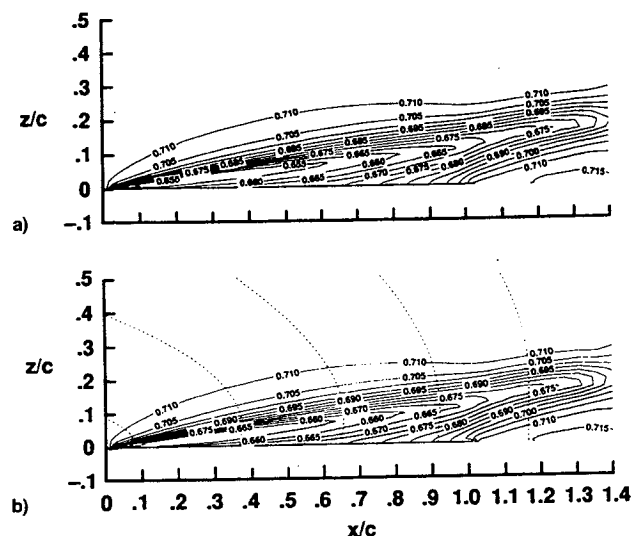


Fig. 9 Computed pressure field in a longitudinal cross section approximately through the vortex core: $M_\infty = 0.3$, $\alpha = 20.5^\circ$, $Re_c = 1 \times 10^6$: a) $112 \times 105 \times 70$ spherical single block grid, b) $112 \times 105 \times 70$ spherical zonal grid.

vortex is not predicted. These comparisons indicate that the $56 \times 54 \times 70$ point grid provides sufficient resolution and accuracy. Therefore, this grid density was used as the basis for comparisons in the rest of this section.

Zonal-Grid Solutions

For the zonal solution the flow domain was divided into zones by partition of the single-block grid starting from the apex and progressing to the trailing edge and the wake. At the interfaces between the zones the grids overlap by one point and they are aligned so that simple injection of boundary information can be used. The solution is advanced one step in the zone at the apex and progresses sequentially from zone to zone until the entire domain is swept. This process is repeated in time until convergence of all zones to a steady state is achieved.

The boundary data are transferred at the interfaces explicitly, and only first-order accuracy is retained at these regions. Transfer of boundary information at flow regions with steep gradients may cause instabilities and discontinuities when large time steps are used. In fact, it was found that the zonal grid solutions required smaller time steps than the single-block solutions in order to retain stability and exhibited slower convergence rates. However, the converged zonal solutions did not have discontinuities, and in terms of accuracy were in agreement with the single-block results. This is demonstrated by the surface pressure distributions shown in Fig. 8 where

results obtained in the single-block $112 \times 105 \times 70$ point spherical grid and the analogous zonal grid are compared. The surface pressure coefficient at $x/c = 0.5$ are in very close agreement. The surface flow patterns (not shown) obtained with the zonal grid were also in good agreement with the patterns computed on the same size single-block grid.

An important consideration for judging accuracy and validity of the zonal solution is the smoothness and accuracy of the solution at the zone interfaces. The continuity of the zonal grid solution is shown in Fig. 9, which presents off-surface pressure contours on an $\eta = \text{const}$ grid surface which passes approximately through the vortex core starting from the apex and extending to the trailing edge. In Fig. 9a the pressure field of the solution obtained on the single-block grid is shown. In Fig. 9b the corresponding zonal-grid solution is shown where the locations of the zonal boundaries are indicated by dashed lines. The two field solutions are seen to be in good agreement.

Effect of Grid Topology

The effect of the grid topology on the solution is examined next and the solutions obtained on spherical and cylindrical grids are compared. The surface pressure coefficients at $x/c = 0.5$ obtained using the cylindrical grid topology are compared to these obtained using a spherical-type grid in Fig. 10. The spherical grid was a $56 \times 54 \times 70$ point single-block grid, while the cylindrical grid was a $57 \times 54 \times 70$ point zonal grid. For most of the spanwise locations the pressure coefficient computed on both type grids agree with each other and with the experiments. However, at the leading edge, $0.95 \leq y/y_{\text{max}} \leq 1$, discrepancies are observed between the two computed solutions. Similar trends are observed for the other axial locations. In the previous paragraph it was shown that the zonal solution method has little effect on the accuracy of

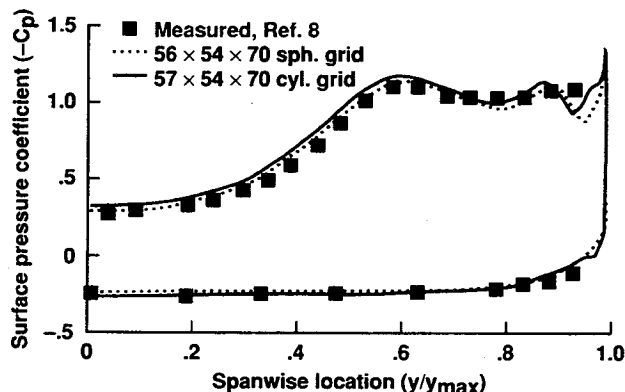


Fig. 10 Effect of the grid topology on the prediction of surface pressure coefficient: $M_\infty = 0.3$, $\alpha = 20.5^\circ$, $Re_c = 1 \times 10^6$.

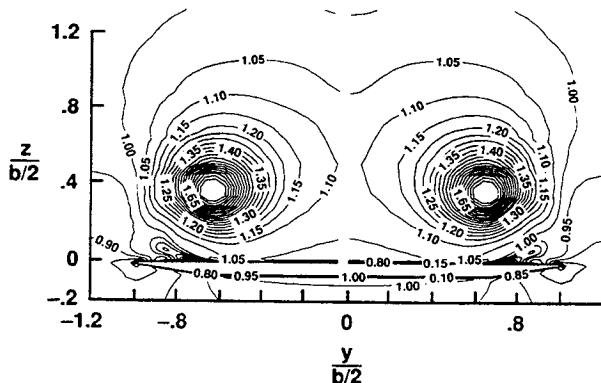


Fig. 11 Computed axial velocity contours at $x/c = 0.9$: $M_\infty = 0.3$, $\alpha = 20.5^\circ$, $Re_c = 1 \times 10^6$, with $57 \times 54 \times 70$ cylindrical zonal grid.

the solution. Therefore, differences between the computed pressures on spherical and cylindrical grids are due to the different approximation of the sharp leading-edge geometry and different spatial distributions of grid points for each grid configuration.

The computed off-surface axial velocity components are presented in Fig. 11 and may be compared with the experimental results of Ref. 9 shown in Fig. 5a. It is observed that the location of the primary vortex core was predicted closely with the cylindrical zonal grid solution, and the computed axial velocities match the experimental results. Solutions on cylindrical grids showed slightly slower convergence rates compared with the solutions on comparable size spherical grids. The slower convergence rate on the cylindrical grids can be attributed to the high grid clustering at the apex region.

Effect of Numerical Algorithm

The sensitivity of the solution on the numerical scheme is examined next. The pressure coefficient at the axial location $x/c = 0.5$ obtained using the central-difference diagonalized scheme¹⁰ is compared with the pressure coefficient predicted using the axially flux-split scheme¹⁴ in Fig. 12. Both solutions were obtained on a $56 \times 54 \times 70$ point single-block spherical grid. The surface pressure coefficient prediction using the diagonalized scheme shows general agreement with the measurements and with predictions of the axially flux-split scheme, for the spanwise locations from the centerline to the location of the suction peak due to the primary vortex. The solution

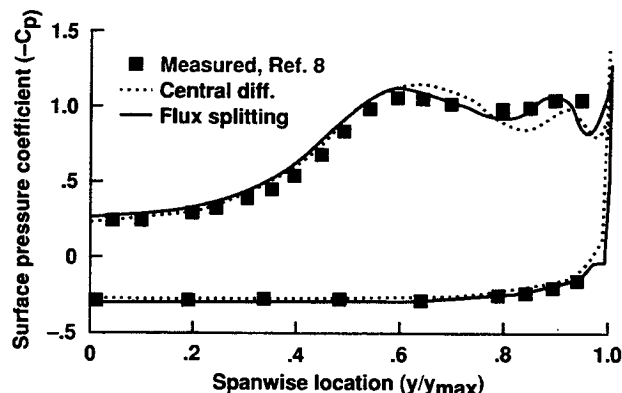


Fig. 12 Effect of the numerical scheme on the prediction of surface pressure coefficient: $M_\infty = 0.3$, $\alpha = 20.5^\circ$, $Re_c = 1 \times 10^6$, solutions on $56 \times 54 \times 70$ spherical grid.

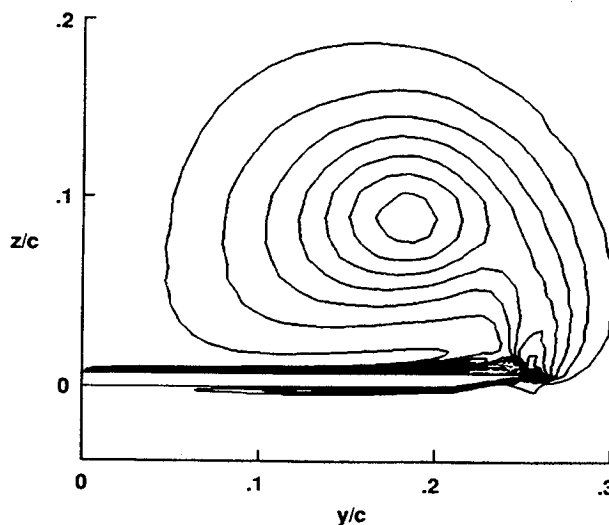


Fig. 13 Helicity contours computed with central-difference diagonalized scheme in the $\xi = \text{const}$ crossflow surface at $x/c = 0.9$: $M_\infty = 0.3$, $\alpha = 20.5^\circ$, $Re_c = 1 \times 10^6$.

with the central-difference scheme did not predict the same location and strength of the suction peaks as the axially flux-splitting scheme.

Figure 13 shows the helicity contours in $\xi = \text{const}$ surface at $x/c = 0.9$. The location of the primary vortices of both solutions are generally in good agreement. However, the secondary vortex obtained with the central-difference solution is located farther outboard and closer to the surface than that of the flux-split solution. The differences in the near-wall flow characteristics can be attributed to the different diffusive characters of the two algorithms used.

Embedded-Grid Solutions

Large portions of the flowfield, such as the windward side flow, are not particularly sensitive to the grid resolution. The basic idea in obtaining solutions with reduction in computing cost, while retaining adequate resolution in critical flow regions, has been to partition the complete domain of the problem into several subdomains. Although it is possible to use partitions intersecting only at the boundaries in the present work, it was decided to use subdomains which overlap. Physical considerations of the flowfield of the present investigation required the use of grid embedding rather than general grid partitioning. The global grid contained $56 \times 54 \times 35$ points and only a portion of this grid on the leeward side was refined along all three coordinate directions. The refined embedded grid (see Fig. 3) included the region of the leading-edge vortices and it extended radially several grid cells beyond the

vortical flow region where significant density and velocity variations are encountered. The portion of the leeward side region with significant density and velocity gradients can be identified by examining the flow solution on the coarse grid. The embedded grid extended spanwise on the leeward side from the symmetry plane to the leading edge. The size of a single-block grid having the equivalent grid resolution of the embedded grid throughout the flow region would be $112 \times 105 \times 70$ points. By using a coarse $56 \times 54 \times 35$ point global and a $80 \times 55 \times 59$ fine embedded grid, the total number of grid points of the global and embedded grid is 2.25 times less than the size of the single-block 112×70 grid.

The surface pressure coefficient at $x/c = 0.5$ is shown in Fig. 14, together with the solution obtained with the $112 \times 105 \times 70$ point single-block grid. The surface pressure coefficient obtained using the baseline $56 \times 54 \times 35$ point grid is also shown. The pressure coefficient obtained by the embedded solution method improved the prediction of the coarse global grid solution, but it did not match the corresponding fine single-block grid solution prediction. The strength and the location of the suction peaks obtained by the embedded grid solution agree with the results obtained with the single-block fine grid solution. However, the surface pressure distribution predictions do not agree for spanwise locations between the suction peaks. It is speculated that closer agreement of the single block and embedded grid solutions would have been obtained if the embedded grid had included part of the leading-edge region on the windward side and part of the wake region. Note also that in Ref. 20, where a grid refinement was employed with another method, a larger part of the leading-edge region was refined.

Comparison between crossflow helicity contours of Fig. 15 and those shown in Fig. 6 demonstrates that the off-surface flow predictions of velocity and density obtained by the embedded and single-block grid solutions are generally in good agreement. The location of the primary vortices obtained by the embedded grid solution agrees closely with those obtained by a single-grid solution and with the location obtained experimentally.

The flow structure of the leeward-side vortical flowfield has two regions which would require fine grid resolution: the boundary-layer region and the vortical flow region including the shear layers emerging from the leading edge. It is possible to refine each of these regions individually. This approach was tried, but the convergence rate was slow, and the flowfield was not smooth at the interfaces of the grids. This was due to the inaccuracy of the interpolation in regions where the flow quantities have rapid spatial variation. Grid refinement for the entire flow region starting from the leeward side surface, and including the leading-edge vortices, was chosen because the interpolation from the global to the refined grid is applied only at the far field where the spatial variation is insignificant.

Flow with Vortex Breakdown

In this section, flows are examined at higher angles of attack where vortex breakdown was observed. The solutions for flows with breakdown were also computed at a freestream Mach number $M_\infty = 0.3$, and $Re_c = 1 \times 10^6$. Detailed experimental data are lacking for flows with vortex breakdown. Most experimental investigations have simply identified qualitative features of the flowfield such as location and extent of vortex breakdown. The numerical solutions indicated that vortex breakdown appears first at an angle-of-attack $\alpha = 32$ deg, as was observed in the experimental investigation of Ref. 21.

Computed Results: $\alpha = 32$ deg

The flow for $\alpha = 32$ deg was computed on a $57 \times 54 \times 70$ point cylindrical grid with the zonal method. The general flowfield characteristics and the vortex breakdown region are shown in Fig. 16. Also shown in Fig. 16a are the pressure contours on the wing surface which indicate the locations of

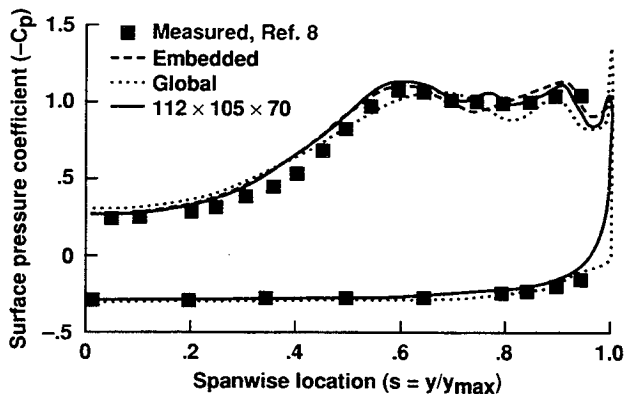


Fig. 14 Surface pressure coefficient with the embedded grid solution: $M_\infty = 0.3$, $\alpha = 20.5$ deg, $Re_c = 1 \times 10^6$.

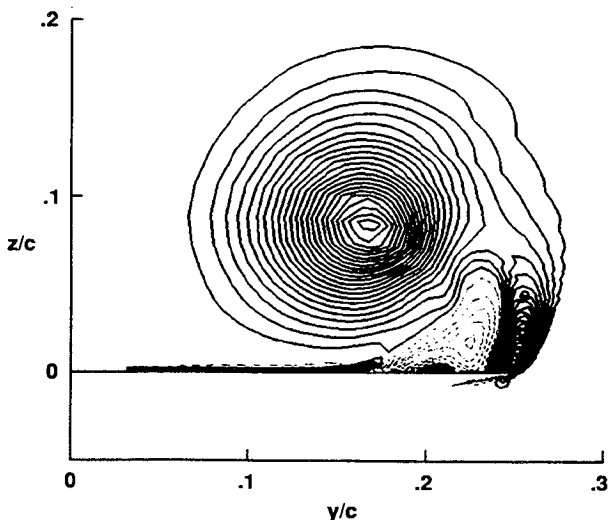


Fig. 15 Helicity contours computed with embedded grids, in the $\xi = \text{const}$ crossflow plane at $x/c = 0.9$: $M_\infty = 0.3$, $\alpha = 20.5$ deg, $Re_c = 1 \times 10^6$.

the primary and secondary suction peaks. The vortex core is shown by streamlines starting from the wing apex, and the approximate shape of the vortical region near the core is shown with the stream surface originating from the leading edge upstream near the apex. The vortex breakdown is shown with the stream surface which has a closed front end (Fig. 16b), indicating the leading edge of the vortex breakdown bubble, and its continuation in the wake. The close-up view shown in Fig. 16b clearly illustrates how the core of the vortex expands and how the flow is diverted downstream of the vortex burst point. It can also be seen in Fig. 17 that the vortex breakdown bubble remains open in the wake region. The vortex breakdown region can be identified using helicity. At the flow reversal region the helicity ($H = \mathbf{V} \cdot \boldsymbol{\Omega}$) changes sign, but also the angle between the velocity and vorticity vectors changes significantly compared with the unburst vortex case. In Fig. 17 the vortex breakdown region in a crossflow plane at $x/c = 0.95$ is identified using the contours of helicity. In the region after breakdown, sudden tilting and rotation of the streamlines causes the angle between the velocity and vorticity vectors to exceed 90 deg. As a result, in the vicinity

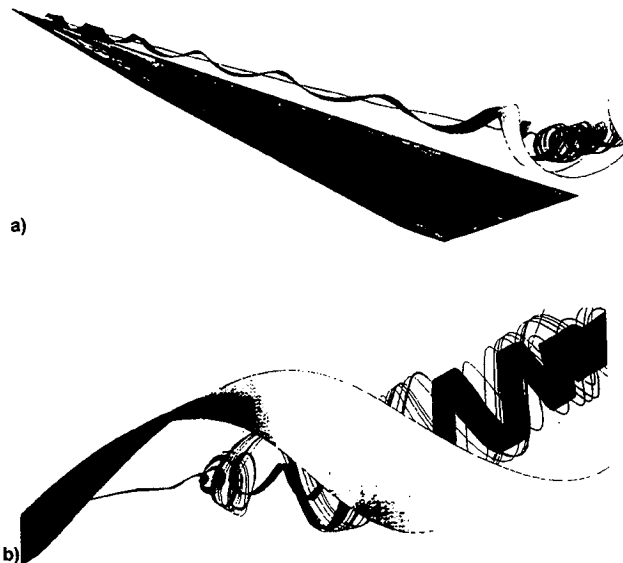


Fig. 16 Vortex core and vortex breakdown region indicated with particle traces: $M_\infty = 0.3$, $\alpha = 32$ deg, $Re_c = 1 \times 10^6$: a) perspective view and b) detail of the vortex breakdown bubble.

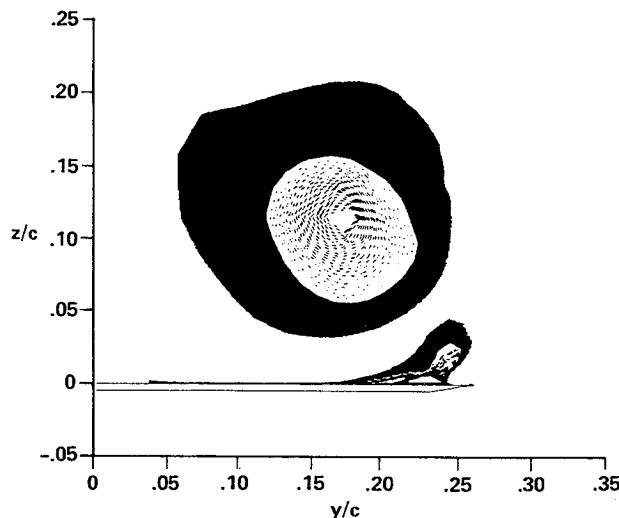


Fig. 17 Computed helicity contours in a cross section through breakdown at $x/c = 0.9$: $M_\infty = 0.3$, $\alpha = 32$ deg, $Re_c = 1 \times 10^6$, with $57 \times 54 \times 70$ grid.

of vortex breakdown the helicity can be negative, even in regions where the velocity vector points downstream and positive in regions where the velocity vector points upstream.

Computed Results: $\alpha = 40$ deg

The computed flow for $\alpha = 40$ deg is presented in Fig. 18. Except where otherwise noted, these results were obtained using a $112 \times 105 \times 70$ point spherical single-block grid. Solutions were also obtained using smaller single-block grids, and the same trends discussed above for the $\alpha = 20.5$ -deg case concerning sensitivity of the solution to grid density also occur at $\alpha = 40$ deg.

The vortex breakdown region for $\alpha = 40$ deg is shown in Fig. 18 using particle traces. Comparing Figs. 18 and 16, we see that at this angle of attack, the vortex burst point is located further forward than at $\alpha = 32$ deg, and the vortex burst is larger.

Vortex breakdown was observed in the solutions for the 75-deg sweep delta wing at $\alpha \geq 35$ deg using grids having a resolution as coarse as $33 \times 54 \times 35$ points. However, the coarse grid solutions tend to predict the vortex burst point further downstream, and a smaller extent of vortex breakdown region than the corresponding fine-grid solutions. Furthermore, when the grid resolution was made even coarser ($33 \times 30 \times 35$ point grid) the vortex breakdown was not observed in the computed solution. These results indicate that the ability to capture vortex breakdown requires a grid fine enough to resolve the features of the off-surface vortex structure, as well as the viscous layers at the body surface.

An important feature governing the occurrence of vortex breakdown on delta wings is the interaction of the vortex with the adverse axial pressure gradient encountered at the wing trailing edge. This sensitivity has been demonstrated in experiments where the downstream pressure has been altered, and was also found in the computations. Vortex breakdown was not obtained when the computational grid excluded the wake region, and thus the adverse pressure gradient developed by the flow downstream of the wing was not present. Similar results were found²² in computations of flow over an aircraft fuselage and wing leading-edge extension at high incidence.

A time-accurate solution was carried out for the $\alpha = 40$ -deg case to investigate possible existence of unsteadiness in the region downstream of the vortex burst point. The solution obtained on the $112 \times 105 \times 70$ point grid was advanced a large number of time steps and the solution examined for

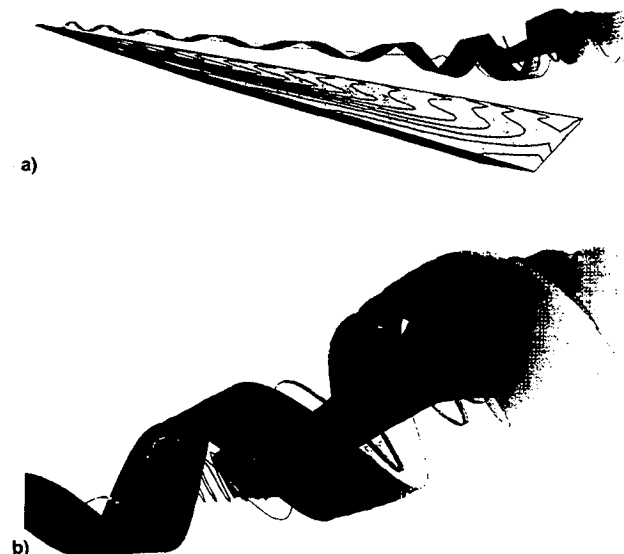


Fig. 18 Vortex core and vortex breakdown region indicated with particle traces: $M_\infty = 0.3$, $\alpha = 40$ deg, $Re_c = 1 \times 10^6$: a) perspective view and b) detail of the vortex breakdown bubble.

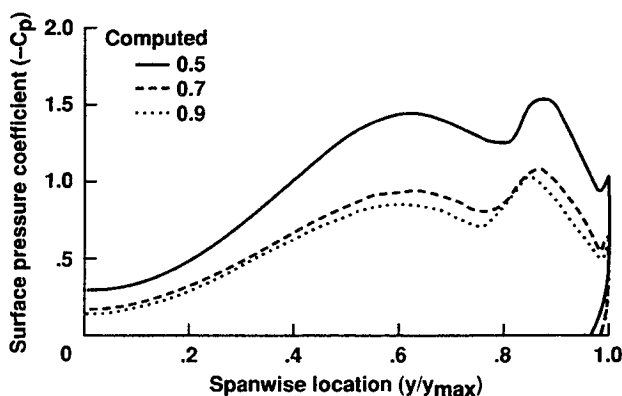


Fig. 19 Surface pressure coefficient upstream of breakdown, close to burst and downstream of burst point: $M_\infty = 0.3$, $\alpha = 40$ deg, $Re_c = 1 \times 10^6$, with $112 \times 105 \times 70$ spherical single-block grid.

evidence of unsteadiness. In the present case the vortex was observed to undergo a bubble-type breakdown, and no unsteadiness was observed in the residuals or in the computed lift or pitching moment. In addition, the computation carried out for a very similar delta wing configuration using a flux-vector-splitting algorithm¹¹ did not reveal the existence of unsteadiness in the computed results. However, numerical investigation of flow over a bubble-delta wing configuration,¹⁰ where spiral type of vortex breakdown was observed at $\alpha = 35$ deg, identified self-excited unsteady flow behavior in that case.

The effect of variation of the angle of attack and the development of vortex breakdown on the aerodynamic behavior of the delta wing can be shown by inspection of the surface pressure distribution. Computed surface pressure distributions at several axial locations for the $112 \times 105 \times 70$ point grid solution at $\alpha = 40$ deg are shown in Fig. 19. Comparison of these surface pressures with the corresponding ones for $\alpha = 20.5$ deg (Fig. 4) gives quantitative information of the effect of vortex breakdown. At $x/c = 0.5$, upstream of the breakdown onset, the suction peak is significantly higher than the one at $\alpha = 20.5$ deg. Vortex breakdown results in significant diminution of the primary suction peaks; the computed surface distribution at $x/c = 0.7$ and $x/c = 0.9$ clearly demonstrates this effect.

Conclusions

The flowfield about a 75-deg sweep delta wing was computed for a range of incidence. At $\alpha = 20.5$ deg the solutions did not exhibit vortex breakdown, and the results were in reasonable agreement with the experiment. It was found that sufficient grid density is required normal to the body surface to resolve the viscous layers adjacent to the body and the leeward-side vortex structures. Solutions were computed with zonal grids and the results were in good agreement with solutions computed on analogous single-block grids. It was found that the grid topology has no significant effect on the accuracy of the solution. The numerical scheme has an effect on the prediction of surface properties and the off-surface field solution. The results of the embedded grid solution were not in perfect agreement with the solutions obtained on fine single-block grids that provide the same resolution as the refined embedded grid, but they improved the solution of the coarser global grid at a smaller computational cost. At higher angles of attack, the computed solutions exhibited vortex breakdown. Bubble-type vortex breakdown was found for the 75-deg sweep delta wing and for angles-of-attack $32 \text{ deg} \leq \alpha \leq 40 \text{ deg}$. Vortex breakdown was predicted on coarse- and fine-

grid solutions. However, adequate grid resolution was found to be important in predicting the correct size and location of the vortex breakdown bubble. The computed flowfield for flow with vortex breakdown did not show unsteadiness even for the finest grid resolution used.

References

- Elle, B. J., "On the Breakdown at High Incidence of the Leading Edge Vortices on Delta Wings," *Journal of the Royal Aeronautical Society*, Vol. 64, Aug. 1960, pp. 491-493.
- Lambourne, N. C., and Bryer, D. W., "The Bursting of Leading-Edge Vortices—Some Observations and Discussion of the Phenomenon," *Aeronautical Research Council Report*, ARC-22775, April 1961.
- Sarpkaya, T., "On Oscillatory and Traveling Vortex Breakdowns," *Journal of Fluid Mechanics*, Vol. 45, Pt. 3, 1971, pp. 545-559.
- Sarpkaya, T., "Vortex Breakdown in Swirling Conical Flows," *AIAA Journal*, Vol. 12, No. 9, 1972, pp. 1792-1799.
- Faler, J. H., and Leibovitch, S., "An Experimental Map of the Internal Structure of a Vortex Breakdown," *Journal of Fluid Mechanics*, Vol. 86, Pt. 2, 1978, pp. 313-335.
- Escudier, M. P., and Zehnder, N., "Vortex Flow Regimes," *Journal of Fluid Mechanics*, Vol. 115, 1982, pp. 105-121.
- Payne, F. M., and Nelson, R. C., "An Experimental Investigation of Vortex Breakdown on Delta Wings," *Vortex Flow Aerodynamics*, NASA CP-2416, Oct. 1985, pp. 135-161.
- Hummel, D., "On the Vortex Formation over a Slender Wing at Large Angles of Incidence," *High Angle of Attack Aerodynamics*, AGARD-CP-247, Paper 15, Jan. 1979.
- Kjelgaard, S. O., and Sellers, W. L., III, "Detailed Flowfield Measurements over a 75-Degree Swept Delta Wing for Code Validation," *Validation of Computational Fluid Dynamics*, Vol. 2, AGARD-CP-437, Paper P10, Dec. 1988.
- Fujii, K., and Schiff, L. B., "Numerical Simulation of Vortical Flows over Strake-Delta Wing," *AIAA Journal*, Vol. 27, No. 9, 1989, pp. 1153-1162.
- Thomas, J. L., Krist, S. T., and Anderson, W. K., "Navier-Stokes Computations of Vortical Flows over Low Aspect Ratio Wings," *AIAA Journal*, Vol. 28, No. 2, 1990, pp. 205-212.
- Kandil, O. A., and Chuang, A. H., "Unsteady Vortex-Dominated Flows Around Maneuvering Wings over a Wide Range of Mach Numbers," *AIAA Paper 88-0317*, Jan. 1988.
- Hartwich, P. M., Hsu, C. H., Luckring, J. M., and Liu, C. H., "Numerical Study of the Vortex Burst Phenomenon for Delta Wings," *AIAA Paper 88-0505*, Jan. 1988.
- Ying, S. X., Steger, J. L., Schiff, L. B., and Baganoff, D., "Numerical Simulation of Unsteady, Viscous High-Angle-of-Attack Flows Using a Partially Flux-Split Algorithm," *AIAA Paper 86-2179*, Aug. 1986.
- Pulliam, T. H., "Artificial Dissipation Models for the Euler Equations," *AIAA Journal*, Vol. 24, No. 12, 1986, pp. 1931-1940.
- Steger, J. L., and Rizk, Y. M., "Generation of Three-Dimensional Body-Fitted Coordinates Using Hyperbolic Partial Differential Equations," *NASA TM 86753*, June 1985.
- Benek, J. A., Buning, P. G., and Steger, J. L., "A 3D Chimera Grid Embedding Technique," *AIAA Paper 85-1523*, July 1985.
- Buning, P. G., Chiu, I. T., Obayashi, S., Rizk, Y. M., and Steger, J. L., "Numerical Simulation of the Integrated Space Shuttle Vehicle in Ascent," *AIAA Paper 88-4359*, Aug. 1988.
- Levy, Y., Degani, D., and Seginer, A., "Graphical Visualization of Vortical Flows by Means of Helicity," *AIAA Journal*, Vol. 28, No. 8, 1990, pp. 1347-1352.
- Fujii, K., "A Method to Increase the Accuracy of Vortical Flow Simulations," *AIAA Paper 88-2562*, June 1988.
- Magness, C., Robinson, O., and Rockwell, D., "Control of Leading-Edge Vortices on a Delta Wing," *AIAA Paper 89-0999*, March 1989.
- Schiff, L. B., Cummings, R. M., Sorenson, R. L., and Rizk, Y. M., "Numerical Simulation of High-Incidence Flow over the Isolated F-18 Fuselage Forebody," *Journal of Aircraft*, Vol. 28, No. 10, 1991, pp. 609-617.